# On Theoretical and Numerical Aspects of the Shape Sensitivity Analysis for the 3D Time-dependent Maxwell's Equations

Stephan Schmidt[1], Maria Schütte[2], and Andrea Walther[2]

August 26, 2015

**Abstract**

We propose a novel approach using shape derivatives to solve inverse optimization problems governed by Maxwell's equations, focusing on identifying hidden geometric objects in a predefined domain. The target functional is of tracking type and determines the distance between the solution of a 3D time-dependent Maxwell problem and given measured data in an $L_2$-norm. Minimization is conducted using gradient information based on shape derivatives. We describe the underlying formulas, the derivation of appropriate upwind fluxes and the derivation of shape gradients for general tracking type objectives and conservation laws. Subsequently, an explicit boundary gradient formulation is given for the problem at hand, leading to structure exploiting data efficient transient adjoints. Numerical results demonstrate the practicability of the proposed approach. Typical applications are non-invasive analysis of diverse materials and remote sensing.

**Keywords:** Maxwell's equations, shape optimization, PDE constrained optimization problem, inverse problems, parameter identification, adjoints

## 1 Introduction

In many research fields such as biology, medical diagnostics, aircraft design, material testing, earth observation and remote sensing, the non-invasive analysis to determine the location and/or structure of a hidden object inside a given material becomes more and more important. In some of these applications, depending on the material and imperfection size, radar measurements, X-Rays or a study of the general electro-magnetic reflection spectra are the appropriate methods of choice. In any case, a problem-dependent target

[1]Universität Würzburg, Germany, stephan.schmidt@mathematik.uni-wuerzburg.de

[2]Universität Paderborn, Germany, [maria.schuette,andrea.walther]@math.uni-paderborn.de

functional constrained by Maxwell's equations has to be solved, which can also be interpreted as an inverse problem. Opposed to standard fluoroscopy and medical imaging, where the object to study is placed between sender and receiver, we are primarily interested in a remote sensing approach, that is a reconstruction mainly based on reflections. Working with a few radiation sources that act as both emitter and receiver, this has the benefit of greatly reducing the experimental setup cost.

So far, quite often the time-dependence of Maxwell's equations has been eliminated using a harmonic formulation, see, e.g., [19, 20]. This includes also a first study on shape sensitivities [5]. However, in a practical setup, one usually faces the propagation of broadband signals and limited abilities to measure the real and imaginary part of the received signal resulting in an ill-posedness of the considered problem. Further difficulties arise when an inclusion has to be determined within a non-stationary process, e.g. within working machinery or within medical imaging problems. Therefore, a solution of the inverse problem in frequency-domain may not be sufficient [1, 17]. Quite recently, there were also a few contributions to the time-dependent optimal control of magnetic fields, see, e.g., [10]. However, to our knowledge, this is the first paper that covers the derivation of shape derivatives for the general case of time-dependent conservation laws, where the domain is the unknown to be found.

With respect to time-dependent simulations, the state-of-the-art approach for large scale applications is to transform the shape identification into a parameter identification problem. Typically, the 'forward' or simulation problem is solved using *Finite Differences in Time Domain* (FDTD) methods on structured grids [18]. Then, the location of objects may be obtained by identifying the material distribution of specific electromagnetic properties over the whole computational domain, see, e.g., [7]. This method is also very successfully applied to antenna design problems [3]. Alternatives include the usage of appropriate indicator functions or phase field methods. Common to all of the above approaches is a representation of the unknown domain or inclusion on a non-matching grid via a smooth, non-sharp interface. Furthermore, this approach transforms the shape optimization problem into a problem of finding a distributed parameter, removing many possibilities for structure exploitations, such as exploiting the existence of boundary representations.

Because we want to identify the actual structure of a hidden object, we conduct a shape sensitivity analysis of the inclusion, allowing direct sharp interface manipulation during an optimization process, thereby operating with a fully resolved boundary on matching meshes. For this purpose, we apply discontinuous Galerkin methods [4] since they have the ability to operate on unstructured grids. Stabilization, inter-element connectivity and implementation of the desired boundary conditions will all be taken care of by considering the characteristic variables and upwind directions of Maxwell's

equations. Conveniently, these characteristic variables will also be crucial for deriving the respective goal function for our optimization problem, an approach previously used in [14] for linear waves and non-inverse problems, only.

The main part of this paper is the proposition of a novel approach to solve the inverse Maxwell problem based on shape optimization. Therefore, a complete analysis of the dependency of the solution on the shape of the geometric object, the scatterer, has to be conducted. One important part of this new approach is the derivation of the shape derivatives for a general conservation law, which is later specialized to Maxwell's equations. For the application of gradient-based optimization methods and the related data management within time-dependent adjoint solvers, a boundary representation of the shape derivative is highly desirable, which is typically called the Hadamard representation of the shape gradient [15]. First analytical results concerning the existence and uniqueness of the local shape derivatives of the Maxwell's equations are stated in [2]. To our knowledge, there exists no comparable work, which contains the derivation of the shape derivatives for the 3D time-dependent Maxwell's equations as well as the numerical analysis part. The forward integration of the state equation is realized using a customized fork of the open source tool Dolfin/FEniCS, see, e.g., [8, 9], which is an efficient standalone tool for PDEs.

The paper is structured as follows: Sec. 2 contains the general formulation for the specific kind of problems which we want to consider and the general form of the shape gradient as well as the one adapted for Maxwell's equations. A description of the 3D time-dependent Maxwell's equations is also given in this section. In Sec. 3 an expression for the upwind fluxes is determined. The analysis of the boundary conditions can be found in Sec. 4. The specific formulation of the target functional and subsequently the derivation of the shape gradient is given in Sec. 5. As a result, we get a representation of the shape gradient in the Hadamard sense, that is a boundary representation. Despite having an explicit form of the gradient, several challenges in computing occur. Solution to these problems as well as numerical results are described in Sec. 6. Two applications examples, the direct measurement of the near field and an example with antenna interaction, are considered in Sec. 7. Finally, conclusions and a short outlook are given in Sec. 8.

## 2 Problem Formulation

We consider a PDE-constrained optimization problem of the type

$$\min_{(\varphi,\Gamma_{inc})} J(\Omega) := \frac{1}{2} \int_{\Gamma_{obs}} \int_{t_0}^{t_f} \|A(n)(\varphi - \varphi_m)\|^2 \, dt dS + \delta \int_{\Gamma_{inc}} 1 \, dS \tag{1}$$

such that

$$\begin{aligned} \dot{\varphi} + \operatorname{div} F(\varphi) &= 0 \quad \text{in } \Omega \times (t_0, t_f) \\ F_b(\varphi, n) &= g \quad \text{on } \Gamma \times [t_0, t_f], \end{aligned} \tag{2}$$

where $\Omega \subset \mathbb{R}^d$ is a bounded domain, $\Gamma_{inc} \subset \Gamma := \partial\Omega$ the boundary of the inclusion and $\Gamma_{obs} \subset \Gamma$ the part of the boundary where observation, i.e., measurements, are taken. Furthermore, $A$ denotes a positive semidefinite matrix, $n$ the outer normal, and $\varphi_m$ the given (experimental) data measured using the actual geometry $\Gamma^*_{inc}$ to be reconstructed. Furthermore, $\delta > 0$ is a regularization parameter, which scales the perimeter penalization. With respect to the underlying PDE, $F$ represents an operator, which does not contain any differentiations. Thus, we consider a purely hyperbolical problem. Appropriate boundary conditions are given by the boundary flux $F_b$, where $g$ describes the sources, i.e., the incoming signal. The variable $t$ lies in the time interval $[t_0, t_f]$ with $0 \leq t_0 < t_f$. A typical outline of the geometry

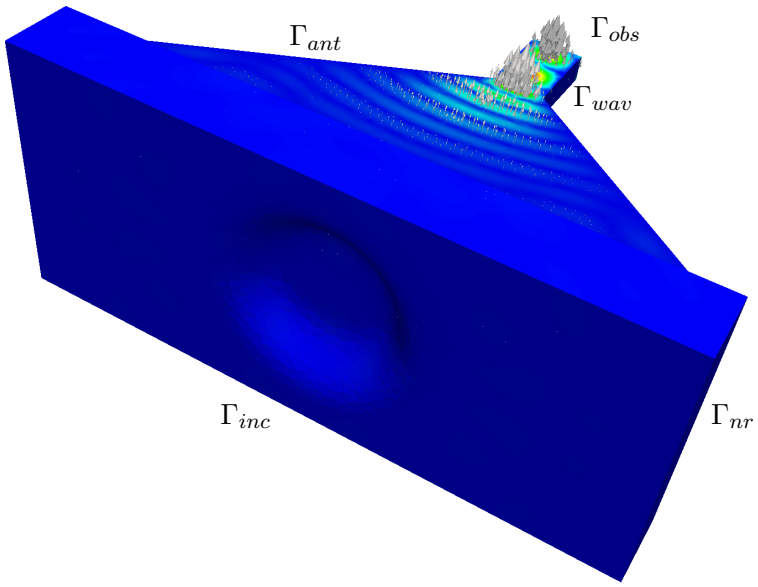


Figure 1: The general layout of the problem: A sender/receiver antenna radiates an inclusion and measures the reflection.

is given by Figure 1, where $\Gamma_{inc}$ denotes the inclusion to be identified. A

wave is both sent and its reflection is received on $\Gamma_{obs}$. Here, the wave first travels through a waveguide $\Gamma_{wav}$ into a typical horn-antenna $\Gamma_{ant}$. Both are thought of as perfect conductors, i.e., to be made of metal. Later on, those perfect conductors will be unified as boundary $\Gamma_E$. The non-reflecting boundary is denoted by $\Gamma_{nr}$.

## 2.1 General Formulation for the Shape Gradient

For optimization purposes, general target functionals like

$$J_1(\Omega) = \int_\Omega h_1(x, \varphi)\ dx \quad \text{or} \quad J_2(\Omega) = \int_\Gamma h_2(s, n, \varphi)\ ds$$

may be used. Let $\Omega \subset D \subset \mathbb{R}^d$ and $V : D \to \mathbb{R}^d$ be a sufficiently smooth vector field describing a deformation of $\Omega$, that is

$$\Omega_\epsilon := \{x + \epsilon V(x) : x \in \Omega\}$$

is a deformed domain for $\epsilon > 0$. Using the Hadamard theorem [15], the shape derivative of $J_1$ at $\Omega$ in direction $V$ is well-known and given by

$$dJ_1(\Omega)[V] = \int_\Gamma \langle V, n\rangle h_1(s, \varphi)\ ds + \int_\Omega h_1'(x, \varphi)\ dx,$$

where $h_1'$ denotes the local shape derivative of $h_1$. Typically, the first part, which is independent of the PDE, is also called the *geometric part*, while the second term, which stems from a variation of the PDE state, is also called the *dynamic part*. Using results from [12] and [16], the shape derivative for the second kind of target functions is of the following form

$$\begin{aligned} &dJ_2(\Omega)[V] = \\ &\int_\Gamma \langle V, n\rangle [\langle \nabla h_2(s, n, \varphi), n\rangle + \kappa(h_2(s, n, \varphi) - D_n h_2(s, n, \varphi) \cdot n) \\ &\qquad + \operatorname{div}_\Gamma(D_n^\top h_2(s, n, \varphi))]\ ds + \int_\Gamma h_2'(s, n, \varphi)\ ds. \end{aligned} \tag{3}$$

Here, $\kappa := \operatorname{div}_\Gamma n$ is $d - 1$ times the mean curvature, with $d$ being the dimension of $\Omega$ and $D_n$ denotes the Jacobian with respect to the component where the normal $n$ is entered. Thus, if $h_2$ is linear in $n$, then the curvature term involving $\kappa$ vanishes and the remaining terms recreate the boundary trace of the 'standard' divergence div from its tangential cousin $\operatorname{div}_\Gamma$, leading to

$$dJ_2(\Omega)[V] = \int_\Gamma \langle V, n\rangle\ \operatorname{div} h_2(s, n, \varphi)\ ds + \int_\Gamma h_2'(s, n, \varphi)\ ds. \tag{4}$$

The shape derivative of the perimeter penalization can directly be found as

$$\int_{\Gamma_{inc}} \langle V, n\rangle \delta\kappa \; dS.$$

Thus, we will focus on the actual tracking type part only. To derive a consistent shape gradient, the weak formulation of the general conservation law Eq. (2) will be used [16]. Using test-functions $\xi$, one has to solve

$$0 = \int_{t_0}^{t_f} \int_{\Omega} \langle \xi, \dot{\varphi}\rangle - \langle F(\varphi), \nabla\xi\rangle \; dxdt + \int_{t_0}^{t_f} \int_{\Gamma} \xi \cdot F_b(\varphi, n) \; dsdt. \tag{5}$$

As can be seen, the first term on the right-hand side resembles $J_1$ and the second term $J_2$. Hence, we obtain the shape linearization of a general conservation law

$$\begin{aligned} 0 = &\int_{t_0}^{t_f} \int_{\Gamma} \langle V, n\rangle \left[\langle \xi, \dot{\varphi}\rangle - \langle F(\varphi), \nabla\xi\rangle\right] \; dsdt + \int_{t_0}^{t_f} \int_{\Gamma} \langle V, n\rangle [\langle \nabla(\xi \cdot F_b(\varphi, n)), n\rangle \\ &+ \kappa \left(\xi \cdot F_b(\varphi, n) - D_n(\xi \cdot F_b(\varphi, n)) \cdot n\right) + \mathrm{div}_{\Gamma}(D_n^{\top}(\xi \cdot F_b(\varphi, n)))] dsdt \\ &+ \int_{t_0}^{t_f} \int_{\Omega} \langle \xi, \dot{\varphi}'\rangle - \langle D_{\varphi}F(\varphi)\varphi', \nabla\xi\rangle \; dxdt + \int_{t_0}^{t_f} \int_{\Gamma} \langle \xi, D_{\varphi}F_b(\varphi, n)\varphi'\rangle \; dsdt. \end{aligned}$$

The variational formulation given by the last equation has to be fulfilled for all suitable test functions $\xi$. Hence, it must also hold for $\lambda$ which will later serve as the adjoint state. The adjoint equation can be found by comparing the derivative of the target function Eq. (1) with respect to the PDE state to the local derivatives of the shape differentiation process. One obtains using integration by parts

$$\begin{aligned} &\int_{t_0}^{t_f} \int_{\Omega} \langle -\dot{\lambda}, \varphi'\rangle - \langle \varphi', D_{\varphi}^{\top}F(\varphi)\nabla\lambda\rangle \; dxdt + \int_{t_0}^{t_f} \int_{\Gamma} \langle \varphi', D_{\varphi}^{\top}F_b(\varphi, n) \cdot \lambda\rangle \; dsdt \\ &+ \int_{t_0}^{t_f} \int_{\Gamma_{obs}} \langle A^{\top}(n)A(n) \cdot (\varphi - \varphi_m), \varphi'\rangle \; dsdt = 0 \end{aligned} \tag{6}$$

and the terminal condition $\lambda(t_f) = 0$, where $\varphi'$ is now the test function. The inhomogenity of the adjoint boundary condition, which stems from the partial derivative of the objective function, can thus not be chosen arbitrarily, rather the choice of $A(n)$ must be consistent with the respective information flow governed by $D_{\varphi}^{\top}F_b(\varphi, n)$. This will be discussed in more detail in Sec. 3. Seeing that the adjoint formulation Eq. (6) requires a gradient operator on

the adjoint state $\lambda$, we will call this the *strong form adjoint*. Likewise, we denote with expression Eq. (7) the *weak form of the adjoint equation*.

$$\begin{aligned}
&\int_{t_0}^{t_f}\int_{\Omega} \langle -\dot{\lambda}, \varphi' \rangle + \langle \operatorname{div}(D_\varphi F(\varphi)\varphi'), \lambda \rangle \; dxdt \\
&\quad + \int_{t_0}^{t_f}\int_{\Gamma} \langle \varphi', D_\varphi^\top F_b(\varphi, n) \cdot \lambda - D_\varphi^\top F(\varphi)\lambda \cdot n \rangle \; dsdt \\
&\quad + \int_{t_0}^{t_f}\int_{\Gamma_{obs}} \langle A^\top(n)A(n) \cdot (\varphi - \varphi_m), \varphi' \rangle \; dsdt = 0.
\end{aligned} \tag{7}$$

The objective function Eq. (1) evaluates the mismatch only on a certain part of the boundary, which is constant and thus does not vary during the optimization process. Consequently, the linearization reduces to the *dynamic part* only. Therefore, one has

$$dJ(\Omega)[V] = \int_{t_0}^{t_f}\int_{\Gamma_{obs}} \langle A^\top(n)A(n) \cdot (\varphi - \varphi_m), \varphi' \rangle \; dsdt,$$

where $dJ(\Omega)[V]$ represents the total derivative with respect to the shape. Now, one can combine Eq. (6) with the shape linearization of a general conservation law given above. If we assume that $F_b(\varphi, n) = \tilde{F}_b(\varphi) \cdot n$, i.e., $F_b(\varphi, n)$ depends only linearly on $n$, and furthermore assume enough regularity of the state $\varphi$, such that there is a respective boundary trace, then the resulting expression simplifies to

$$dJ(\Omega) = \int_{t_0}^{t_f}\int_{\Gamma_{obs}} \langle V, n \rangle \operatorname{div}(D_n^\top(\lambda \cdot \tilde{F}_b(\varphi) \cdot n)) \; dsdt. \tag{8}$$

## 2.2 Adaptation for Maxwell's Equations

From now on, we assume that the state equation in the PDE-constrained optimization problem is given by the time-dependent Maxwell's equations, i.e., one has

$$\begin{aligned}
\frac{\partial B(t,x)}{\partial t} &= -\nabla \times E(t,x) \\
\frac{\partial D(t,x)}{\partial t} &= \nabla \times H(t,x) - \sigma E \\
\nabla \cdot D(t,x) &= \rho \\
\nabla \cdot B(t,x) &= 0,
\end{aligned}$$

where $x \in \Omega$, $B(t,x)$ describes the magnetic flux density, $E(t,x)$ the electric flux strength, $D(t,x)$ the time-dependent displacement of the current and $H(t,x)$ the magnetic flux strength. The related material equations for linear, isotropic and non-dispersive media are defined by

$$D = \varepsilon E \quad \text{and} \quad B = \mu H,$$

with $\varepsilon = \varepsilon_0 \varepsilon_r$ and $\mu = \mu_0 \mu_r$, where $\varepsilon_0$ and $\mu_0$ are the constant vacuum permittivity and permeability. Furthermore, $\varepsilon_r$ and $\mu_r$ denote the relative, material dependent, counterparts, which may vary over the domain for different applications. The same is true for $\sigma$, which describes the conductivity. Coupling Faraday's law and Ampere's law with the material equation yields

$$\begin{aligned} \mu \frac{\partial H}{\partial t} &= -\nabla \times E \\ \varepsilon \frac{\partial E}{\partial t} &= \nabla \times H - \sigma E. \end{aligned}$$

For a complete problem formulation, appropriate boundary conditions containing also the incoming pulse must be defined. They are derived in detail in Sec. 4.

# 3 Upwinding and Transport of Information

We have to distinguish between reflections and primary waves. A convenient way of accomplishing this is the consideration of an upwinding approach. Therefore, we will choose our measurement operator $A(n)$ to coincide with the positive definite part of the upwind splitting of the conservation law, which enables us to identify the information flow through facets. This is conform with the information flow of the adjoint. Since the consideration of upwinding is already necessary for our modeling approach, the discretization by a discontinuous Galerkin method suggests itself.

To apply discontinuous Galerkin methods, a variational formulation for Maxwell's equations given by

$$\int_{t_0}^{t_f} \int_{\Omega} v^\top \cdot \left( \frac{\partial H}{\partial t} + \frac{1}{\mu} \operatorname{curl} E \right) + w^\top \cdot \left( \frac{\partial E}{\partial t} - \frac{1}{\varepsilon} \operatorname{curl} H + \frac{\sigma}{\varepsilon} E \right) \, dx dt = 0$$

is needed, where $v$ and $w$ are the test functions. Integration by parts for the

curl operator yields

$$\begin{aligned}\int_{t_0}^{t_f}\int_{\Omega}&\langle v,\frac{\partial H}{\partial t}\rangle+\langle E,\frac{1}{\mu}\operatorname{curl} v\rangle\\&+\langle w,\frac{\partial E}{\partial t}\rangle-\langle H,\frac{1}{\varepsilon}\operatorname{curl} w\rangle+\frac{\sigma}{\varepsilon}\langle w,E\rangle dxdt\\-\int_{t_0}^{t_f}\int_{\Gamma}&\frac{1}{\mu}\langle v,E\times n\rangle-\frac{1}{\varepsilon}\langle w,H\times n\rangle dsdt=0.\end{aligned}\tag{9}$$

Furthermore, a discretization of the considered domain is required. Therefore, from now on $\Omega_h$ represents a polygonal triangulation of $\Omega$ defining also the physical outer boundary $\Gamma$ and inner inter-element interfaces $S$. To obtain the general form as stated in Sec. 2, we first define

$$A_n := \begin{bmatrix} 0 & -n_z & n_y \\ n_z & 0 & -n_x \\ -n_y & n_x & 0 \end{bmatrix}.$$

We use the above definition likewise for different components, such as $A_E$ or $A_H$. It is worth noting that for any vector $v$ one has

$$A_n v = n\times v = -v\times n = A_{-v}n = -A_v n = -A_n^\top v.$$

Then Eq. (9) can be expressed inline with the general expression Eq. (5):

$$\begin{aligned}&\int_{t_0}^{t_f}\int_{\Omega_h}\langle v,\frac{\partial H}{\partial t}\rangle+\frac{1}{\mu}\langle A_E,\nabla v\rangle+\langle w,\frac{\partial E}{\partial t}\rangle-\frac{1}{\varepsilon}\langle A_H,\nabla w\rangle+\frac{\sigma}{\varepsilon}\langle w,E\rangle dxdt\\&-\int_{t_0}^{t_f}\int_{\Gamma}(v,w)F_b(H,E,n)dsdt-\int_{t_0}^{t_f}\int_{S}(v,w)F_S(H,E,n)dsdt=0,\end{aligned}\tag{10}$$

where

$$F_S(H,E,n)=\bar{A}\begin{pmatrix}H\\E\end{pmatrix}\quad\text{with}\quad\bar{A}=\begin{bmatrix}0&-\frac{1}{\mu}A_n\\\frac{1}{\varepsilon}A_n&0\end{bmatrix}$$

and the inner product for matrices $\langle A_E,\nabla v\rangle$ is interpreted as the componentwise sum.

To derive the upwind scheme, the matrix $\overline{A}$ must now be split in a positive and negative semidefinite part. For this purpose, the diagonalization is a convenient tool. For the projection onto the space of eigenvectors of $\overline{A}$, one has the eigenvalues

$$c_1=0,\ c_2=0,\ c_3=-\frac{1}{\sqrt{\mu\varepsilon}},\ c_4=-\frac{1}{\sqrt{\mu\varepsilon}},\ c_5=\frac{1}{\sqrt{\mu\varepsilon}},\ c_6=\frac{1}{\sqrt{\mu\varepsilon}}$$

of $\overline{A}$ with the eigenvectors

$$
\begin{aligned}
v_1 &= \left( \; 0,0,0,n_x,n_y,n_z \; \right)^\top, \qquad v_2 = \left( \; n_x,n_y,n_z,0,0,0 \; \right)^\top, \\
v_3 &= \left( \; -\sqrt{\tfrac{\varepsilon}{\mu}}n_x n_y, \sqrt{\tfrac{\varepsilon}{\mu}}(n_x^2+n_z^2), -\sqrt{\tfrac{\varepsilon}{\mu}}n_y n_z, -n_z, 0, n_x \; \right)^\top, \\
v_4 &= \left( \; \sqrt{\tfrac{\varepsilon}{\mu}}n_x n_z, \sqrt{\tfrac{\varepsilon}{\mu}}n_y n_z, -\sqrt{\tfrac{\varepsilon}{\mu}}(n_x^2+n_y^2), -n_y, n_x, 0 \; \right)^\top, \\
v_5 &= \left( \; \sqrt{\tfrac{\varepsilon}{\mu}}n_x n_y, -\sqrt{\tfrac{\varepsilon}{\mu}}(n_x^2+n_z^2), \sqrt{\tfrac{\varepsilon}{\mu}}n_y n_z, -n_z, 0, n_x \; \right)^\top, \\
v_6 &= \left( \; -\sqrt{\tfrac{\varepsilon}{\mu}}n_x n_z, -\sqrt{\tfrac{\varepsilon}{\mu}}n_y n_z, \sqrt{\tfrac{\varepsilon}{\mu}}(n_x^2+n_y^2), -n_y, n_x, 0 \; \right)^\top.
\end{aligned}
$$

To simplify notation we will use throughout the abbreviations

$$
Y = \sqrt{\frac{\varepsilon}{\mu}}, \quad Z = \sqrt{\frac{\mu}{\varepsilon}}, \quad \text{and} \quad c = \frac{1}{\sqrt{\mu\varepsilon}}.
$$

Using the similarity transformation

$$
\Lambda = P^{-1}\overline{A}P,
$$

where

$$
\begin{aligned}
P &:= [v_5, v_3, v_1, v_6, v_4, v_2] \\
&= \begin{bmatrix}
n_x n_y Y & -n_x n_y Y & 0 & -n_x n_z Y & n_x n_z Y & n_x \\
-(n_x^2+n_z^2)Y & (n_x^2+n_z^2)Y & 0 & -n_y n_z Y & n_y n_z Y & n_y \\
n_y n_z Y & -n_y n_z Y & 0 & (n_x^2+n_y^2)Y & -(n_x^2+n_y^2)Y & n_z \\
-n_z & -n_z & n_x & -n_y & -n_y & 0 \\
0 & 0 & n_y & n_x & n_x & 0 \\
n_x & n_x & n_z & 0 & 0 & 0
\end{bmatrix},
\end{aligned}
$$

one gets the diagonal representation $\Lambda = \operatorname{diag}(c, -c, 0, c, -c, 0)$, i.e., the diagonal elements of $\Lambda$ are given by the corresponding eigenvalues. Defining the new operators $A^{\pm} = P\Lambda^{\pm}P^{-1}$, where $\Lambda^{+} = \operatorname{diag}(\max(c_i, 0))$ and $\Lambda^{-} = \operatorname{diag}(\min(c_i, 0))$, it is easy to see that $\overline{A}$ can be split into

$$
A^{+} = \frac{1}{2}\begin{bmatrix} \tilde{A}_n c & A_n Y c \\ -A_n Z c & \tilde{A}_n c \end{bmatrix}, \quad A^{-} = \frac{1}{2}\begin{bmatrix} -\tilde{A}_n c & A_n Y c \\ -A_n Z c & -\tilde{A}_n c \end{bmatrix},
$$

i.e., a positive semidefinite part and a negative semidefinite part, where

$$
\tilde{A}_n := \begin{bmatrix} n_y^2+n_z^2 & -n_x n_y & -n_x n_z \\ -n_x n_y & n_x^2+n_z^2 & -n_y n_z \\ -n_x n_z & -n_y n_z & n_x^2+n_y^2 \end{bmatrix}
$$

and $A_n$ is defined as above. Furthermore, $\tilde{A}_n v = n \times (v \times n) = -A_n^2 v$. Thus, we specify a stabilized form of Eq. (10) by setting

$$\begin{aligned} F_S(H,E,n) &= \overline{A} \cdot \begin{pmatrix} H \\ E \end{pmatrix} = \begin{bmatrix} 0 & -\frac{1}{\mu} A_n \\ \frac{1}{\varepsilon} A_n & 0 \end{bmatrix} \begin{pmatrix} H \\ E \end{pmatrix} \\ &= (P \Lambda P^{-1}) \cdot \begin{pmatrix} H \\ E \end{pmatrix} \\ &\doteq \left[ (P \Lambda^+ P^{-1}) \cdot \begin{pmatrix} H^l \\ E^l \end{pmatrix} + (P \Lambda^- P^{-1}) \cdot \begin{pmatrix} H^r \\ E^r \end{pmatrix} \right] \\ &= \frac{1}{2} \left[ \begin{bmatrix} \tilde{A}_n c & A_n Y c \\ -A_n Z c & \tilde{A}_n c \end{bmatrix} \cdot \begin{pmatrix} H^l \\ E^l \end{pmatrix} \right. \\ &\quad \left. + \begin{bmatrix} -\tilde{A}_n c & A_n Y c \\ -A_n Z c & -\tilde{A}_n c \end{bmatrix} \cdot \begin{pmatrix} H^r \\ E^r \end{pmatrix} \right], \end{aligned}$$

where $^l$ stands for the local unknowns and $^r$ for the remote unknowns. This general expression $F_S(H,E,n)$ of the upwind scheme will now be modified to create expressions for $F_b(H,E,n)$, specifying the boundary conditions holding on the respective surfaces.

# 4 Boundary Conditions

Up to now, $\Gamma$ comprises all physical boundaries, which are now split into parts $\Gamma_E$ orthogonal to the $E$ field, $\Gamma_H$ orthogonal to the $H$ field, $\Gamma_{obs}$ defining the entering pulse and also the area where the measurements take place, and $\Gamma_{nr}$ for the remaining absorbing, i.e., nonreflecting, boundary. Symmetry boundaries are likewise given by $\Gamma_E$ and $\Gamma_H$. Metallic surfaces such as the considered obstacle $\Gamma_{inc}$ are modeled as perfect conductors and are also contained in $\Gamma_E$. Thus, with respect to the geometry shown in Figure 1, we have $\Gamma_E = \Gamma_{inc} \cup \Gamma_{ant} \cup \Gamma_{wav}$, as all of these boundaries are thought of as perfectly conducting metals.

First, we exploit for $\Gamma_E$ that $A_n E = 0$, meaning the electric field must not have a tangential component. This yields

$$\begin{aligned} F_b^E(H,E,n) &= \frac{1}{2} \begin{bmatrix} \tilde{A}_n c & A_n Y c \\ -A_n Z c & \tilde{A}_n c \end{bmatrix} \cdot \begin{pmatrix} H \\ E \end{pmatrix} \\ &\quad + \frac{1}{2} \begin{bmatrix} -\tilde{A}_n c & A_n Y c \\ -A_n Z c & -\tilde{A}_n c \end{bmatrix} \cdot \begin{pmatrix} H \\ E \end{pmatrix} \\ &= \begin{bmatrix} 0 & 0 \\ -A_n Z c & 0 \end{bmatrix} \cdot \begin{pmatrix} H \\ E \end{pmatrix} = \begin{pmatrix} 0 \\ -A_n Z c H \end{pmatrix}. \end{aligned} \tag{11}$$

Likewise, one obtains for $\Gamma_H$ with $A_n H = 0$

$$F_b^H(H,E,n) = \begin{bmatrix} 0 & A_n Y c \\ 0 & 0 \end{bmatrix} \cdot \begin{pmatrix} H \\ E \end{pmatrix} = \begin{pmatrix} A_n Y c E \\ 0 \end{pmatrix}.$$

For $\Gamma_{inc}$, one can define the following boundary conditions

$$\begin{aligned} F_b^{inc}(H,E,n) = \frac{1}{2}\begin{bmatrix} \tilde{A}_n c & A_n Y c \\ -A_n Z c & \tilde{A}_n c \end{bmatrix} \cdot \begin{pmatrix} H \\ E \end{pmatrix} \\ + \frac{1}{2}\begin{bmatrix} -\tilde{A}_n c & A_n Y c \\ -A_n Z c & -\tilde{A}_n c \end{bmatrix} \cdot \begin{pmatrix} g_H \\ g_E \end{pmatrix}. \end{aligned} \tag{12}$$

For non-reflective boundaries $\Gamma_{nr}$, the same flux holds with $g_H = g_E \equiv 0$.

# 5 Derivation of the Shape Gradient

Our goal is to determine the actual structure of a hidden object inside a given domain. Based on an initial geometry, the forward simulation is performed and the reflected electric and magnetic fields are simulated and measured on the surface $\Gamma_{inc}$. To get an analytical expression for the simulated field values, we only consider the part leaving the computational domain, which is the first term on the right-hand side of Eq. (12). Consequently, we obtain

$$A(n) := \frac{1}{2}\begin{bmatrix} \tilde{A}_n c & A_n Y c \\ -A_n Z c & \tilde{A}_n c \end{bmatrix},$$

which forms the right-hand side in the adjoint equation (6). For the shape derivative without the regularization parameter $\delta$, we insert the function $F_b^E$ into the shape gradient (8) arriving at

$$\begin{aligned} dJ(\Omega) &= \int_{t_0}^{t_f} \int_{\Gamma_{obs}} \langle V, n\rangle \operatorname{div}(D_n^\top (\lambda \cdot \tilde{F}_b(H,E)\cdot n))\; dsdt \\ &= \int_{t_0}^{t_f} \int_{\Gamma_{obs}} \langle V, n\rangle \operatorname{div}(D_n^\top\, (\lambda_E \cdot (-A_n Z c H)))\; dsdt \\ &= \int_{t_0}^{t_f} \int_{\Gamma_{obs}} \langle V, n\rangle Zc \operatorname{div}(\lambda_E \times H)\; dsdt, \end{aligned} \tag{13}$$

where we exploited that the differentiation of $A_n$ with respect to the normal $n$ yields the cross product.

# 6 Implementations

## 6.1 The Primal Solver

To solve Maxwell's equations, we employ a discontinuous Galerkin scheme on an unstructured tetrahedral mesh using the boundary and upwind stabilization fluxes as described in Sec. 3 and 4. Although the use of higher

order test- and ansatz-functions can be quite beneficial, we limit ourselves to straight sided tetrahedrons. Thus, in order to get a high resolution of the domain, which directly corresponds to the resolution of our unknown domain to be found, we use first order test- and ansatz-functions and rather prefer spatially refined meshes over higher polynomial degrees, as otherwise we would have a low resolution of the geometry unless we were to incorporate curved elements in both the simulation and shape optimization components. Time derivatives are discretized using Crank–Nicolson, which for a linear problem such as Maxwell's equations also coincides with the implicit midpoint rule. Thus, our time integration is symplectic but we need to solve an implicit system for each time-step, which is done in distributed memory parallelism using GMRES preconditioned by a parallel ILU solver, a functionality offered by PETSc and Hypre Euclid, which is based on the PILU algorithm [6].

## 6.2 The Adjoint Solver

Following the same argumentation as when deriving Eq. (6) and taking into account the linear nature of the problem, it is easy to see that the volume part of the strong form adjoint is given by the problem to find $(\lambda_H, \lambda_E)$, such that

$$\begin{aligned} 0 = \int_{t_0}^{t_f} \int_{\Omega} & \langle \lambda_H, \frac{\partial H'}{\partial t} \rangle + \langle E', \frac{1}{\mu} \operatorname{curl} \lambda_H \rangle \\ & + \langle \lambda_E, \frac{\partial E'}{\partial t} \rangle - \langle H', \frac{1}{\varepsilon} \operatorname{curl} \lambda_E \rangle + \frac{\sigma}{\varepsilon} \langle \lambda_E, E' \rangle dx dt, \end{aligned} \tag{14}$$

and consequently the volume component of the weak form of the adjoint is given by

$$\begin{aligned} 0 = \int_{t_0}^{t_f} \int_{\Omega} & \langle v, \frac{\partial \lambda_H}{\partial t} \rangle + \langle \lambda_E, \frac{1}{\varepsilon} \operatorname{curl} v \rangle \\ & + \langle w, \frac{\partial \lambda_E}{\partial t} \rangle - \langle \lambda_H, \frac{1}{\mu} \operatorname{curl} w \rangle - \frac{\sigma}{\varepsilon} \langle \lambda_E, w \rangle dx dt, \end{aligned} \tag{15}$$

where we have reintroduced the symbols $(v, w)$ for the test-functions and flipped the signs due to time reversal. Comparing the time-corrected weak form of the adjoint (15) with its primal counterpart (9), one can see that the same solver can be used, provided some signs and coefficients $\mu$ and $\epsilon$ are swapped correctly.

We will now discuss the adjoint boundary fluxes exemplified by boundary $\Gamma_E$. From Eq. (6) and Eq. (11) we see that the strong form boundary flux

for $\Gamma_E$ is given by

$$0 = \int_{t_0}^{t_f} \int_{\Gamma_E} (H', E') \begin{bmatrix} 0 & A_n Zc \\ 0 & 0 \end{bmatrix} \cdot \begin{pmatrix} \lambda_H \\ \lambda_E \end{pmatrix} \, dsdt,$$

where we have used the anti-symmetry of $A_n$. Although this suggests at first glance that electric and magnetic boundary conditions swap, the impression changes when considering the extra boundary terms due to moving to the weak form:

$$\begin{aligned} 0 &= \int_{t_0}^{t_f} \int_{\Gamma_E} (v, w) \left( \begin{bmatrix} 0 & -A_n Zc \\ A_n Yc & 0 \end{bmatrix} + \begin{bmatrix} 0 & A_n Zc \\ 0 & 0 \end{bmatrix} \right) \cdot \begin{pmatrix} \lambda_H \\ \lambda_E \end{pmatrix} \, dsdt \\ &= \int_{t_0}^{t_f} \int_{\Gamma_E} (v, w) \begin{bmatrix} 0 & 0 \\ A_n Yc & 0 \end{bmatrix} \cdot \begin{pmatrix} \lambda_H \\ \lambda_E \end{pmatrix} \, dsdt. \end{aligned}$$

Thus, the same solver with the same boundary fluxes can again be used, provided one takes into account swapping $\epsilon$ and $\mu$.

### 6.2.1 Adjoint Data Management

Since the gradient formulation (13) is also based on the corresponding adjoint formulation, one faces as always the problem to store the state of the forward problem that is needed for the backward integration of the adjoint equation (6). Since we consider the three dimensional time-dependent case, the storage of the full trajectory would cause a tremendous memory requirement, too large even for todays high-performance computing infrastructure.

However, due to the special problem structure here, paired with the boundary representation of the shape gradient, only a fraction of the data needs to be stored. In particular, we only need the offset of the simulated primal state $(H, E)$ on the sender/receiver boundary $\Gamma_{obs}$ to generate the respective forcing

$$\int_{t_0}^{t_f} \int_{\Gamma_{obs}} \langle A^\top(n) A(n) \cdot (H - H^m, E - E^m)^\top, (v, w)^\top \rangle \, dsdt \tag{16}$$

of the adjoint. In order to actually compute the gradient, we furthermore need the primal state only in the first cell layer around $\Gamma_{inc}$, such that the trace of the volume divergence in Eq. (13) can be computed correctly. This leads to a tremendous reduction in data, such that no checkpointing is needed. For all test-cases considered as part of this work, the system RAM suffices to store all necessary data. Furthermore, we use a highly robust CVT-based mesh deformation [13], such that all meshes, meaning the

mesh for generating the reference solution, the initial mesh and all meshes generated during optimization, are topologically equivalent with the same connectivity. Because $\Gamma_{obs}$ is fixed, the offset, Eq. (16), can always be evaluated without interpolation. Furthermore, we can reuse some structures of the ILU elimination process because the non-zero pattern never changes between test-cases.

### 6.3 Computing Curvature and the Gradient

Implementing the evaluation of the shape derivative poses additional challenges, in particular the curvature computation for the regularization parameter. To this end, we fully utilize the possibility of FEniCS to solve PDEs on manifolds [11]. To this end, we extract all relevant boundary meshes from the volume mesh. On these boundary meshes, we then compute a vertex normal within the space of continuous first order vector finite element ansatz-functions. Afterwards, we compute $\kappa = \operatorname{div}_\Gamma n$ by solving

$$\int_\Gamma vu \; dS = \int_\Gamma v \operatorname{div}_\Gamma n \; dS$$

for ansatz-functions $u$ and testfunctions $v$ within the finite element space of continuous first order functions within the tangent plane to $\Gamma$. The boundary trace of the volume divergence in Eq. (13) is conveniently computed by first applying the standard FEM divergence operator in the volume and then selecting the respective degrees of freedom on the boundary.

In addition to having a regularization parameter $\delta$ in Eq. (1), we conduct our gradient descent scheme in the space $H^1$, meaning that the shape derivative $dJ$ from Eq. (13) is projected into the space $H^1$ by solving

$$(\delta_S \Delta_\Gamma + I) dJ_S = -dJ$$

on the boundary $\Gamma_{inc}$, where $I$ is the identity. For all our applications, we set $\delta_S = 10^{-3}$. In each optimization step, we then update the domain in accordance to

$$\Gamma_{inc}^{k+1} := \{x + \tau \cdot dJ_S : x \in \Gamma_{inc}^k\},$$

where $\tau$ is the step-length of the gradient descent scheme.

## 7 Numerical Results

### 7.1 Near-Field Reconstruction

Our first test-case is the reconstruction of an obstacle by prescribing and measuring the near-field pulse. The base geometry is a rectangular cuboid

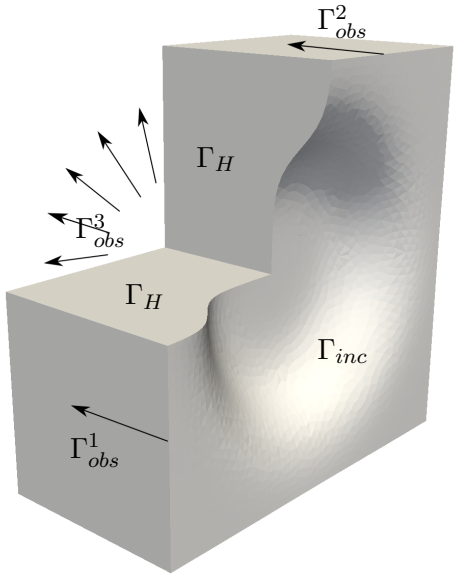


Figure 2: Cut through the near-field test-case. Black arrows symbolize the incoming electric field. Corresponding magnetic field not shown.

of 24 cm by 24 cm by 12 cm edge length, where the rear side is deformed by the sigmoid function

$$z_{new} = z + \frac{-W}{2 + 2\exp\left(100(\sqrt{x^2+y^2} - W)\right)},$$

where $W = \frac{299\,792\,458\,\mathrm{m\,s^{-1}}}{4.1\,\mathrm{GHz}} \approx 7.31\,\mathrm{cm}$ is the wavelength of a sinusoidal pulse at 4.1 GHz, which creates a smooth bump of roughly 3.65 cm elevation on the rear side of the cuboid. These numbers are chosen such that the physical dimensions of the inclusion are within the centimeter magnitude, which will be the natural wavelength for the antenna we are going to consider in the second test-case. The domain is shown in Figure 2. We want to exploit the symmetry of this domain by computing only a quarter section. Because the obstacle $\Gamma_{inc}$ supposed to be illuminated is a perfect conductor, only orthogonal electric fields can traverse over $\Gamma_{inc}$. Thus, we send two linearly polarized electromagnetic fields originating from $\Gamma^1_{obs}$ and $\Gamma^2_{obs}$. Consequently, the symmetry planes need to be of $\Gamma_H$-type, leaving only the possibility to send a radially polarized wave from $\Gamma^3_{obs}$.

The amplitude as a function of time of the incoming scanning signals is the same truncated SINC-pulse for all boundaries $\Gamma^1_{obs}$, $\Gamma^2_{obs}$ and $\Gamma^3_{obs}$, namely

$$g(t) = \frac{\sin\big(2\pi f_s(t-t_c)\big)}{2\pi f_s(t-t_c)} \sin\big(2\pi f_c(t-t_c)\big) w(t,t_c), \tag{17}$$

to be multiplied with the respective vectors determining the base polariza-

tion. Here, $t_c$ is the time around which the pulse is centered, $f_c$ is the desired center frequency, $f_s$ is the half bandwidth of the signal. We set $t_c = 3/(2f_s)$ and use the Hamming window function

$$w(t, t_c) = \begin{cases} 0.54 + 0.46 \cos\left(\frac{\pi(t-t_c)}{t_c}\right), & \text{for } t \in [0, 2t_c], \\ 0, & \text{otherwise.} \end{cases} \tag{18}$$

In particular, our center frequency equals $f_c = 8.2\,\text{GHz}$ and the spread is $f_s = 4.1\,\text{GHz}$, meaning we scan using frequencies ranging from 4.1 GHz to 12.3 GHz. With respect to wavelengths, this corresponds to using waves ranging between 2.4 cm and 7.3 cm, the same order of magnitude as the 3.65 cm bump. To accurately resolve these waves, we operate at time-steps of 6.1 ps. We terminate the simulation after 3.336 ns. This is the time the electromagnetic wave needs to travel 1 m and with a domain size of 12 cm we assume that all reflections have been captured by then. Both reconstructed

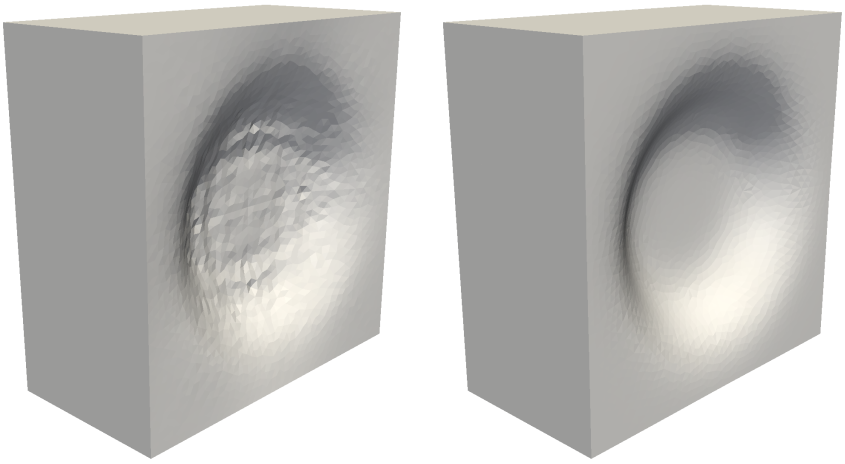

Figure 3: Reconstruction after 373 optimization steps (left) vs. target shape (right).

and target shape are shown in Figure 3 and their cross-sections are shown in Figure 4, where we have started from a flat backside. Furthermore, a perimeter penalization of $\delta = 5 \cdot 10^{-5}$ is used in Eq. (1). It is worth noting that for smaller values of $\delta$ the optimization usually converged to a local optimum with clear discrepancy in both the electromagnetic reflection of the reconstruction as well as the actual geometry. Finally, the development of the signal offset, that is the value of Eq. (1) without the perimeter penalty term, is shown in Figure 5. Considering that the global optimum of zero signal offset is obtainable, the achieved objective value is very promising. In an actual application, the regularization parameter $\delta$ would probably needed to be reduced in a homotopy fashion, matching the signal offset even better than

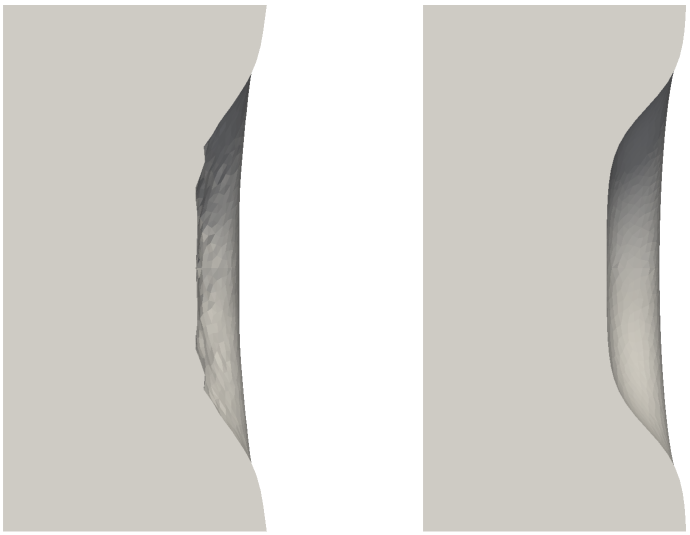

Figure 4: Cross-sectional comparison between reconstruction and target.

the already achieved $9.22 \cdot 10^{-2}$ as shown in Figure 5. Comparing both the

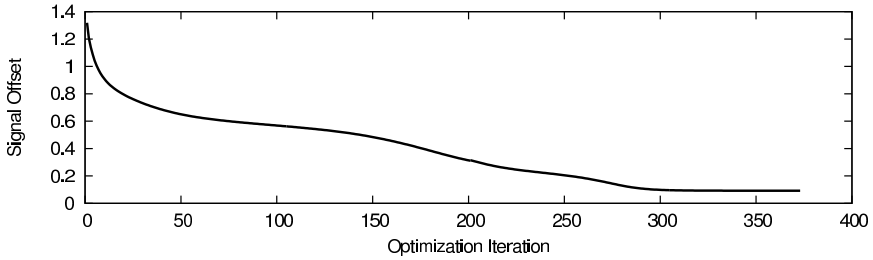


Figure 5: Signal offset during optimization.

signal offset and the actual geometry, we conclude that the reconstruction has worked surprisingly well in this near-field example, opening the possibility to actually include the antenna interaction as a second test.

## 7.2 Reconstruction with Horn Antenna

The second test-case is the reconstruction of an obstacle including the actual antenna geometry. To this case, we enhance the obstacle as given in Sec. 7.1 with a waveguide and a horn antenna, which acts as both emitter and receiver, creating the geometry as depicted in Figure 1. The waveguide geometry matches an E-band WR229 waveguide, that is 2.29 inches $\times$1.15 inches or 5.8166 cm $\times$ 2.921 cm. Attached to this waveguide is a standard gain horn modeled after the Pasternack PE9862-20, which is 59.563 cm long

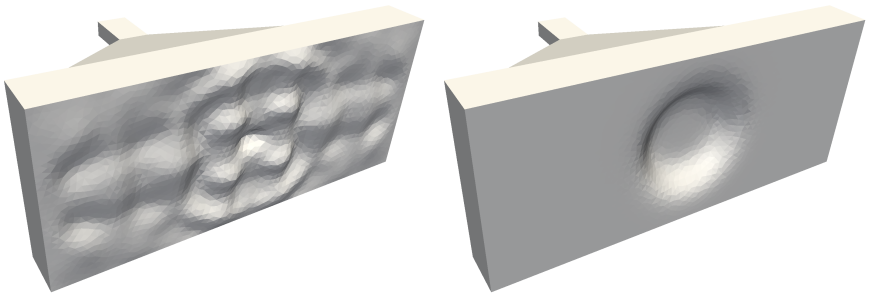

Figure 6: Reconstructed and target shape for the horn antenna test-case after 376 optimization iterations.

and has a mouth of 31.496 cm × 22.225 cm. It is worth noting that contrary to the near-field situation in Sec. 7.1, the horn antenna and waveguide in this setup acts as a polarization filter, allowing only linearly polarized waves to pass through. The ideal frequency range for this antenna ranges from 3.3 GHz to 4.9 GHz. As such, we use the same truncated SINC-pulse as in

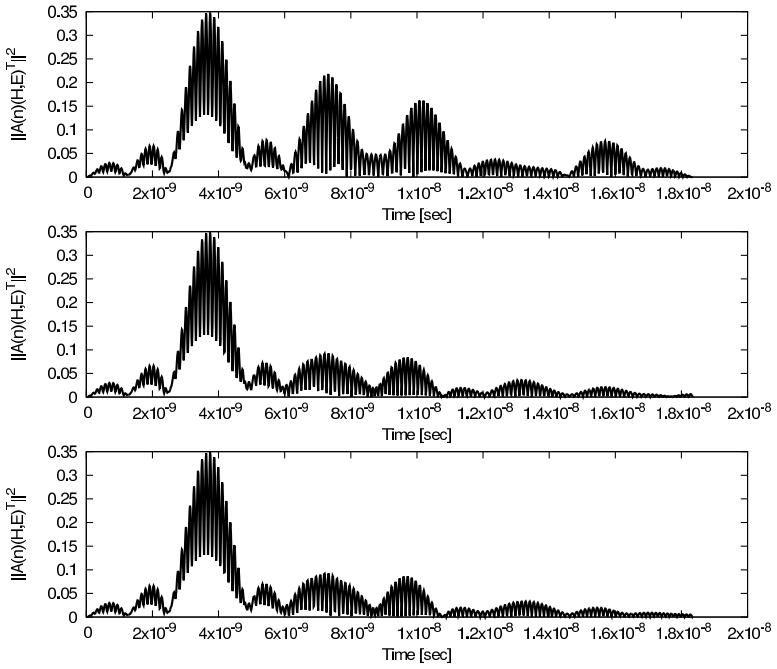


Figure 7: Reflections of the initial geometry, the optimized geometry and the reference.

Eq. (17) and Eq. (18), but with a center frequency of $f_c = 4.1$ GHz and a spread of 0.41 GHz, which puts us well within the optimal frequency range

of this antenna setup. As mentioned above, the corresponding wavelength is 7.31 cm, which is roughly twice the size of the bump depth. Reconstructed and target inclusion are shown in Figure 6. For this application, the penalty term $\delta$ in Eq. (1) is set to zero. Although there is a clear visual discrepancy between the reconstructed and desired shape, the actual signals as measured by the antenna coincide very well, see Figure 7. As in the near-field case, the initial geometry here is a flat plate. Comparing this result with the near-field test, we can see that this particular experiment involving a horn antenna is not the ideal approach, most likely due to the polarization filtering effect of the receiver. However, the very successful near-field reconstruction suggests the feasibility of the method and as part of future studies, we will include the antenna shape as an optimization variable, leading to a approach involving optimal design of experiments and optimization under uncertainties for these reconstruction problems.

# 8 Conclusions and Outlook

A novel methodology to solve time-dependent hyperbolic inverse shape optimization problems has been considered, based on tracking the information flow identified via upwinding. Exploiting the nature of such shape optimization problems by considering a boundary representation of the gradient allows a considerable amount of data reduction for the backwards-in-time transient adjoint. Furthermore, direct sharp interface reconstruction based on deforming physical boundaries synergises very well with discontinuous Galerkin methods and the upwind flux modeling of the tracking. The problem is first considered on a general level and then specialized to Maxwell's equations. After discussing a discontinuous Galerkin Maxwell solver and its adjoint on unstructured tetrahedral meshes, we conclude with two numerical test-cases: The reconstruction of a bump based on near-field information and with the inclusion of a complete horn antenna setup. The near-field example is very promising, reconstructing not only the simulated and measured information, but also the actual geometry. When including the horn antenna, we still manage to get a very good signal match, but the geometries are noticeably different, probably due to the polarization filtering and narrow frequency band of the waveguide and horn antenna. For both problems, we see an excellent convergence behavior of a $H^1$-gradient descent scheme. Future work will be focused on including the antenna geometry into the optimization problem, thereby finding experimental setups that manage to recreate the very good match of the near-field problem also in the more realistic antenna case.

The authors gratefully acknowledge the support of the Federal Ministry of Education and Research (BMBF) within the project HPC-FLiS under the support code 01 IH 11 009.

## References

[1] E. Abenius. Time-domain inverse electromagnetic scattering using FDTD and gradient-based minimization. Licentiate Thesis, 2004.

[2] J. Cagnol, J.P. Marmorat, and J.P. Zolésio. Shape sensitivity analysis in the Maxwell's equations. In J. Cagnol, M.P. Polis, and J.P. Zolesio, editors, *Shape Optimization And Optimal Design*, Lecture notes in pure and applied mathematics. Taylor & Francis, 2001.

[3] E. Hassan, E. Wadbro, and M. Berggren. Topology optimization of metallic antennas. *IEEE Transactions on Antennas and Propagation*, 62(5):2488 – 2500, 2014.

[4] J.S. Hesthaven and T. Warburton. *Nodal Discontinuous Galerkin Methods: Algorithms, Analysis, and Applications*. Springer, 2008.

[5] M. Hintermüller, A. Laurain, and I. Yousept. Shape sensitivities for an inverse problem in magnetic induction tomography based on the eddy current model. *Inverse Problems*, 31:065006, 2015.

[6] D. Hysom and A. Pothen. A scalable parallel algorithm for incomplete factor preconditioning. *SIAM Journal on Scientific Computing*, 22(6):2194–2215, 2001.

[7] D. Landmann, D. Plettemeier, C. Statz, F. Hoffeins, U. Markwardt, W. Nagel, A. Walther, A. Herique, and W. Kofman. Three-dimensional reconstruction of a comet nucleus by optimal control of Maxwell's equations: A contribution to the experiment CONSERT onboard space craft Rosetta. In *Proceedings of the IEEE International Radar Conference*, pages 1392–1936, 2010.

[8] A. Logg, K.A. Mardal, and G.N. Wells, editors. *Automated Solution of Differential Equations by the Finite Element Method*, volume 84 of *Lecture Notes in Computational Science and Engineering*. Springer, 2012.

[9] A. Logg, G.N. Wells, and J. Hake. *DOLFIN: a C++/Python Finite Element Library*, chapter 10. Springer, 2012.

[10] S. Nicaise, S. Stingelin, and F. Tröltzsch. Optimal control of magnetic fields in flow measurement. *Discrete and Continuous Dynamical Systems. Series S*, 8(3):579–605, 2015.

[11] M. E. Rognes, D. A. Ham, C. J. Cotter, and A. T. T. McRae. Automating the solution of PDEs on the sphere and other manifolds in FEniCS 1.2. *Geoscientific Model Development*, 6:2099–2119, 2013.

[12] S. Schmidt. *Efficient Large Scale Aerodynamic Design Based on Shape Calculus*. PhD thesis, University Trier, 2010.

[13] S. Schmidt. A two stage CVT / eikonal convection mesh deformation approach for large nodal deformations. eprint arXiv:1411.7663, 2014.

[14] S. Schmidt, E. Wadbro, and M. Berggren. Large-scale three-dimensional acoustic horn optimization. Technical report, 2015. (submitted).

[15] J. Sokolowski and J.P. Zolésio. *Introduction to Shape Optimization: Shape Sensitivity Analysis*. Springer, 1992.

[16] M. Sonntag, S. Schmidt, and N. Gauger. Shape derivatives for the compressible Navier–Stokes equations in variational form. eprint arXiv:1312.5861 (submitted), 2013.

[17] A. Taflove and S. Hagness. *Computational Electrodynamics: The Finite-Difference Time-Domain Method*. Artech House Publishers, 2005.

[18] A. Taflove and S.C. Hagness. *Computational Electrodynamics: The Finite-Difference Time-Domain Method, Third Edition*. Artech House, 3 edition, 2005.

[19] R.N. Klupp Taylor, F. Seifrt, O. Zhuromskyy, U. Peschel, G. Leugering, and W. Peukert. Painting by numbers: Nanoparticle-based colorants in the post-empirical age. *Advanced Materials*, 23(22-23):2554–2570, 2011.

[20] I. Yousept. Optimal control of Maxwell's equations with regularized state constraints. *Computational Optimization and Applications*, 52(2):559–581, 2012.